Applied Surface Science 616 (2023) 156441

Contents lists available at ScienceDirect

Applied Surface Science

journal homepage: www.elsevier.com/locate/apsusc

Full Length Article

Desalination behavior of composite membrane with petal shaped pore—formed by superimposition of covalent organic framework with large aperture difference

Mengjiao Guan [a,1], Dengfeng Yang [a,1], Qing Li [c], Huiting Zhang [a], Jianan Xu [d], Mengmeng Cai [a], Weike Lin [a], Shengqian Ma [b,*], Qingzhi Liu [a,*]

[a] College of Chemistry and Pharmaceutical Science, Qingdao Agricultural University, Qingdao 266109, Shandong, China
[b] Department of Chemistry, University of North Texas, 1508W Mulberry St, Denton, TX 76201, United States
[c] College of Chemical and Biological Engineering, Shandong University of Science and Technology, Qingdao 266590, Shandong, China
[d] School of Chemical Engineering, Northwest University, Xi'an, Shanxi 710069, China

ARTICLE INFO

Keywords:
Covalent organic framework
Different apertures
Desalination
Molecular simulation

ABSTRACT

Covalent organic frameworks (COFs) are promising materials for developing the new generation of reverse-osmosis membranes owing to their unique structure with well-defined nanoporosity and highly tunable pore-wall chemistry. In this work, a new separation membrane was developed using the molecular dynamics (MD) simulation method by superimposing two COF-based films: HPB-COF (0.577 nm) and TpPa-1 (1.582 nm), with a large difference in aperture. The results showed that the new double-layer superimposition membrane could overcome the trade-off effect, and achieve a high water flux and salt rejection rate. According to the membrane model microanalysis, the HPB-COF divided TpPa-1 into six "petals", thus endowing the first layer and second layer of the membrane with a larger accessible surface area and smaller effective pore diameter, respectively. As a result, the new composite membrane simultaneously had combined advantages of the two COF materials. The water permeance of the TpPa-1/HPB-COF composite membrane was 1.85 times higher than that of the AB-stacked HPB-COF membrane, which was two orders of magnitude higher than that of other conventional reverse-osmosis membranes. The salt rejection rate was 100%, which was higher than that of AB-stacked TpPa-1 membrane (39.42%). Furthermore, the microanalysis revealed that the hydrophilic C═O in TpPa-1 positively improved the water flux.

1. Introduction

Global awareness of fresh water scarcity has attracted the attention of most governments [1–3]. Many countries are currently faced with the challenge of obtaining fresh water from seawater to address water shortages. To date, various desalination methods, including distillation [4–6]. electrolysis [7,8], forward osmosis (FO) [9,10] and reverse osmosis (RO) [11–13], have been developed. Among these methods, reverse-osmosis technology is known as "seawater purification technology" in the twenty-first century owing to its advantages of low energy consumption, wide application range, and convenient operation. It is also the mainstream technology used for alleviating the global water crisis [14–16].

RO is a membrane-separation technology that uses on a porous membrane to separate solvents and solutes in solutions under pressure. The properties of RO membranes mainly determine the separation performance of RO desalination [17,18]. To date, membrane materials still cannot break the trade-off effect, thus making it is difficult to obtain high water flux while maintaining the high ion rejection rate [19,20]. As a result, further study on new reverse-osmosis membranes that can achieve higher water flux while maintaining a high salt rejection rate is necessary.

With the development of nanomaterials, their smooth surfaces and atom-sized nanopores have received significant interest as potential separation membranes in recent years [21–25], and are expected to break the trade-off effect [26]. Covalent organic framework (COF)-based

* Corresponding authors.
E-mail addresses: shengqian.ma@unt.edu (S. Ma), qzliu@qau.edu.cn (Q. Liu).
[1] The two author contributed equally in this article.

https://doi.org/10.1016/j.apsusc.2023.156441
Received 21 November 2022; Received in revised form 1 January 2023; Accepted 13 January 2023
Available online 18 January 2023

nanomaterials have a unique structure with well-defined nanoporosity and highly tunable pore-wall chemistry, which can be predesigned to meet different needs [27–30]. Most COFs have an aperture of about 0.6–10.0 nm [31], however, membranes commonly used for desalination require smaller apertures to ensure efficient capturing of ions. Hence, researchers have made efforts to develop COF-based membranes with the requirements of excellent desalination performance. Huang [32] et al. synthesized the IISERP-COOH-COF1 via a ring-opening reaction to study the modified groups on desalination performance. They found that the pore aperture was constricted through post-modification, thus preventing the ions from passing through the membranes. Jiang [1] et al. investigated the effect of different functional groups on desalination performance. They confirmed that hydrophilic functional groups contribute to the increased of water flux. Further, Wang [33] et al. reported that the offset channel at the interface of bilayers obtained from the secondary growth of the COF could significantly enhance ion-separation performance. Wang [34] et al. computationally constructed single- and multilayered TpPa-1 COFs to investigate the influence of multilayered TpPa-1 COFs on the transport behavior of water and salt ions. The NEMD simulation results showed that the ion rejection rate increased with the number of the stack layers at the expense of water permeation. In 2019, Wang [35] et al. constructed a series of CTF multilayers and found that the AB-stacking mode reduced the equivalent pore size, thus improving ion rejection but lowering permeation.

In addition to the salt rejection rate, the water permeation rate is also an important indicator for evaluating the performance of the membrane, i.e., achieving a high salt rejection rate while maintaining high water flux. A study was conducted to investigate the effect of graphene nanopores with different geometries on desalination performance, and the result showed that graphene nanopores with irregular elongated geometries exhibited superior performance. The superior performance of the graphene nanopores was attributed to the smaller equivalent pore size and larger pore area [36]. As a result, we doubted if this phenomenon could be used to improve the desalination performance of COF membranes. Jiang [29] et al. synthesized bilayer COF membranes composed by COF monolayer with different functional groups. Xu et al. successfully exfoliated the TpPa-2 into nanosheets that can match the thickness of Polyamide (PA) layer [37]. Metal tetraphenylporphyrin-based COF (MTPP–COF) monolayer was successfully prepared by laminar assembly and interfacial polymerization [38]. Wang [33] et al. proposed the secondary growth strategy is developed to build bi-layered COF nanofilms. All the above mentioned studies show that that single-layer or double-layer COFs films are feasible in experiments, providing technical support for synthesizing the composite membrane. In addition, the membrane prepared by TpPa-1 showed good performance in long-term stability tests, and its properties remained very stable after soaking in acidic and alkaline solutions [39].

To date, most related studies focused on the addition of functional groups to COF and the stacking of COF with similar pore sizes. However, there are still no relevant reports on the desalination performance of composite membranes with different pore sizes. Thus, in this work, composite membrane with small-pore HPB-COF (0.577 nm) and large-pore TpPa-1 (1.582 nm) was constructed with irregular pores are formed in the composite membrane. The desalination performance of the composite membrane was evaluated using MD simulation and compared with AB-staked bilayers. The TpPa-1/HPB-COF composite membrane achieved a 100 % ion rejection rate and maintained higher water permeability. The composite membrane was characterized using a series of analyses. The TpPa-1/HPB-COF layer spacing effect on desalination performance was explored. Therefore, our design work for single-layer, double-layer and multi-layer COFs films has high experimental guidance value.

2. Methods

Fig. 1(a-c) shows that HPB-COF [40], MPCOF [41], and TpPa-1 [42] with their effective pore sizes: 0.577, 0.978, and 1.582 nm, respectively. They were selected as representatives of different pore sizes to study their various capacities for desalination. Their structures were obtained from the CoRE COF database [43], constructed according to the experimental studies. As shown in Fig. 1d, the typical desalination model was developed. The model comprised a feed side (saline water with 0.599 mol/L NaCl [44–46]), permeate side (pure water), and a COF membrane. The model also contained two rigid graphene sheets. The graphene plate on the feed side acted as a piston, applying a pressure ranging from 50.1 to 200.1 MPa. The graphene plate on the permeate side can apply a pressure of 0.1 MPa to maintain water density and system stability in the simulation process. Taking the TpPa-1 model as an example, the xy plane of the simulation box was 37.692 × 33.838 $Å^2$, 4260 water molecules, 46 Na^+, and 46 Cl^- formed the feed side of 0.599 mol/L NaCl solution with a length of 100 Å along the Z-axis. The permeate side contained 426 water molecules, with a length of 10 Å along the Z-axis.

All simulations were performed using the large-scale atomic/molecular massively parallel simulator (LAMMPS) package [47]. The water model of SPC/E [48] was selected because its diffusion coefficient was close to the experiment value, and the SHAKE algorithm was used to sustain the rigidity of the water molecules and save simulation time. Nonbonding interactions are calculated using Equation (1):

$$\sum 4\varepsilon_{ij}\left[\left(\frac{\sigma_{ij}}{r_{ij}}\right)^{12}-\left(\frac{\sigma_{ij}}{r_{ij}}\right)^{6}\right]+\sum\frac{q_i q_j}{4\pi\varepsilon_0 r_{ij}} \quad (1)$$

where the ε_{ij} and σ_{ij} represent the well depth and collision diameter respectively, the q_i and q_j denote partial charge of atoms i and r in order, the r_{ij} indicates the distance between atoms i and j. The cutoff of the electrostatic interaction distance was set to 1.0 nm, and that of the Lennard-Jones (LJ) was set to 1.2 nm. The LJ parameters for the membrane atoms were obtained from the Dreiding force field [43,49,50], which were successfully used in simulations of COF or metal organic framework (MOF) materials. The other ions were taken from a previous study [51], and the details of about parameters are displayed in Table. S1. The Lorentz–Berthelot mixing rule was adopted for all pairwise LJ terms. The atomic partial charges were described using electrostatic potential (ESP) charges, which were calculated using the grid-based ChelpG algorithm based on the density functional theory (DFT) [35]. Periodic boundary conditions were used in all three directions. The particle–particle–particle-mesh method (PPPM) was used to calculate the long-range electrostatic interactions with an accuracy of 10^{-4} [35]. The Nosé–Hoover thermostat was used to modulate the temperature at 300 K in the simulation process. For each simulation, energy minimization and equilibrium MD simulation were first performed to equilibrate the model system. Then, a 20 ns NVT simulation was performed to estimate the water flux and ion rejection rate under 50 MPa. The external pressure is calculated using Equation (2):

$$f=\frac{PA}{n} \quad (2)$$

Where A is the surface area of the piston, and n is the number of atoms that makes up the piston. The high pressure is often used in MD simulations [34,35], and the reason for the externally applied pressure in the piston is set much higher than the actual value to reduce thermal noise, which ensures accurate values within a limited time scale of a nanosecond. The time step was set to 1 fs, and the data were captured every 1000 steps. To verify the accuracy of the result, the simulation of TpPa-1/HPB-COF was repeated, and the result is shown in Fig. S2.

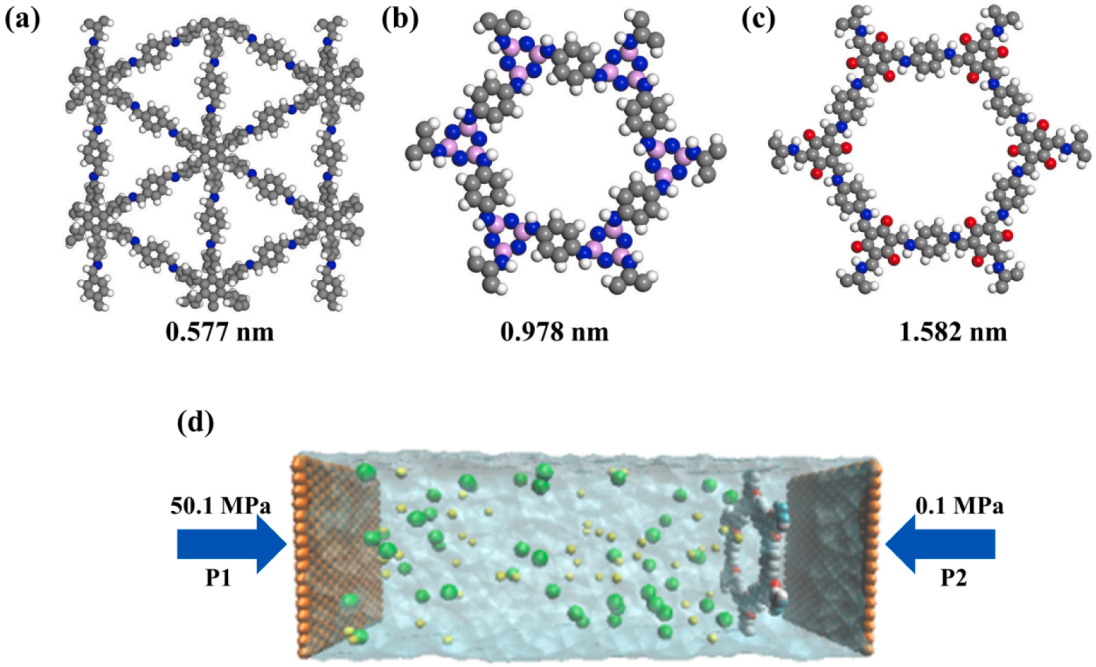

Fig. 1. Topological scheme of (a) HPB-COF, (b) MPCOF, and (c) TpPa-1 membrane, (d) A typical desalination model embraces two compartments along with the RO membrane. Atom color codes: water (transport blue), Na^+ (yellow), Cl^- (green), and carbon in the two sheets of graphene at the box: edges (brown). (For interpretation of the references to color in this figure legend, the reader is referred to the web version of this article.)

3. Result and discussion

3.1. Water permeation and salt rejection capacity of HPB-COF, MPCOF, and TpPa-1 monolayers

The performance of HPB-COF, MPCOF, and TpPa-1 monolayers as RO membranes under 50 MPa hydrostatic pressures was investigated, and the change in the amount of water entering the permeate sides with time is shown in Fig. S1. As shown in Fig. 2(a), the magnitude of the water permeance mainly depended on pore size. Among these materials, HPB-COF had the smallest pore size, and the water permeation rate was 73.34 L/cm^2/day/MPa, while that of the TpPa-1 was 629.15 L/cm^2/day/MPa, which is about 8.6 times that of HPB-COF. Another important criterion for evaluating membrane performance is ion rejection, which is calculated using Equation (3):

$$R = 1 - \frac{C_p}{C_f} \tag{3}$$

where C_p is the ratio of the number of ions passing through the membrane into the permeation side to the number of water molecules, and the C_f is the initial ion concentration at the feed side. In terms of ion interception, HPB-COF had the most outstanding performance, reaching 59.83%, the ion interception rate of MPCOF was 20.56%, and TpPa-1 could not capture ions. Consistent with the conventional view, COF with a larger pore size improves water permeance, while COF with a smaller pore size has a better ion trapping effect. The above results showed that the studied COF monolayer alone is insufficient to achieve the desired desalination effect. By considering the experimental feasibility of multilayer COF materials and the possibility of improving desalination performance, it is necessary to conduct the research on multilayer superimposed COF materials.

3.2. Transport resistance of AB-Stacked COF bilayer

To improve the ion rejection rate of the three COF membranes, the AB-stacking mode was selected to examine the desalination performance of the staggered COF bilayer membranes with the same pore size. The interlayer spacing of the constructed bilayers was adjusted to 0.34 nm (based on the nearest carbon atom between two layers) to eliminate the influence of layer spacing, which was set according to the experimental

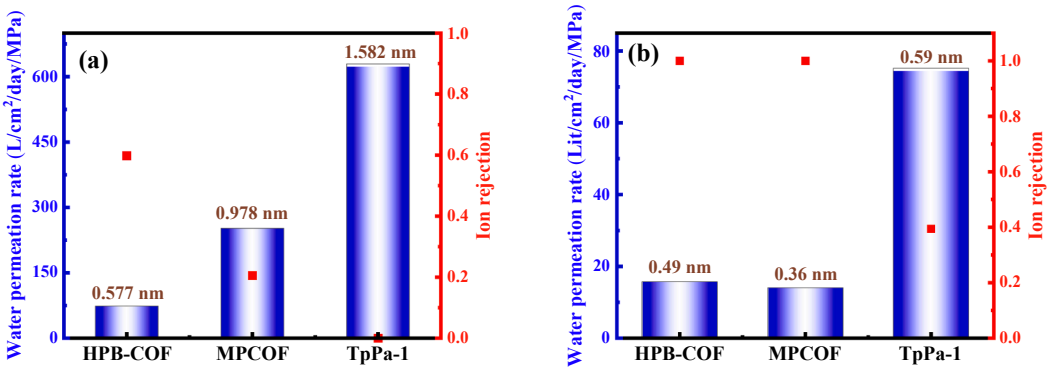

Fig. 2. Water permeation rate and ion rejection rate of (a) HPB-COF, MPCOF, and TpPa-1 monolayers membrane and (b) AB-stacked HPB-COF, MPCOF, and TpPa-1 bilayer membrane.

data of TpPa-1 double-layer membrane. The construction of AB-stacked HPB-COF, MPCOF, and TpPa-1 bilayer membranes is shown in Fig. 3. The equivalent pore diameters of the AB-stacked HPB-COF, MPCOF, and TpPa-1 bilayer membranes were reduced to 0.49, 0.36, and 0.59 nm, respectively, using Zeo++ software [52]. The hole of MPCOF was divided into three small regular pores, while the AB-stacked HPB-COF exhibited a large rhombic pore and two small triangular pores, which resulted in the larger equivalent pore size of AB-stacked HPB-COF. As expected, the AB-stacking mode significantly contributed to the improvement in ion rejection rate. AB-stacked HPB-COF and MPCOF exhibited excellent ion repellency (about 100% desalination). As shown in Fig. S4, when AB-stacked HPB-COF and MPCOF were used as RO membranes, almost all ions stayed in the feed chamber, and only a few ions entered the membrane region. However, the ion rejection rate (39.42%) of the AB-stacked TpPa-1 bilayer was unsatisfactory. Furthermore, more ions flowed through the membrane and eventually entered the pure water side, indicating that "AB-stacking" might not be suitable for large-pore COFs. However, the AB-stacking mode has a significant negative effect on water infiltration. As shown in Fig. 2b, the water permeability of HPB-COF, MPCOF, and TpPa-1 bilayer membranes decreased to 15.72, 14.06, and 75.19 L/cm^2/day/MPa.

3.3. Transport resistance of different types of COF stacks

By placing TpPa-1 on the feed side, the HPB-COF and TpPa-1 were stacked as a composite RO membrane (denoted as TpPa-1/HPB-COF) to investigate whether they could be used to achieve higher water flux while maintaining a high salt rejection rate than using AB-stacked HPB-COF and MPCOF. As shown in Fig. 4(a), each large pore of TpPa-1 was segmented into six "petals" with HPB-COF, and the equivalent pore diameter was reduced to 0.525 nm, which is 12% less than the AB-stacked TpPa-1. Then, the desalination performance of the composite membrane under different pressure was then tested, and the water permeation rate of the membrane as a function of ΔP was plotted (Fig. 4d). As the pressure increased from 50 to 200 MPa, the water flux increased from 125 to 473 #/ns, which positively correlated with ΔP. When the pressure was below 200 MPa, the salt rejection rate of TpPa-1/HPB-COF remained above 90%. As the external pressure increased, the water flux linearly increased, while the salt rejection rate decreased to some extent due to higher ΔP leading to stronger dehydration of ions [35]. The results showed that the TpPa-1/HPB-COF membrane exhibited better desalination performance at lower pressure, indicating that the composite membrane would exhibit superior performance under lower experimentally applied external pressure. Compared with the original AB-stacked HPB-COF, the water flux is increased by 1.85 times, and the salt rejection rate still remains 100 % under 50 MPa. Compared with the original AB-stacked TpPa-1 membrane, the salt rejection rate of the TpPa-1/HPB-COF membrane significantly improved, meaning that COF superimposed by large and small pore sizes simultaneously improved water flux and salt interception rate.

3.3.1. Ion rejection

To further explore the superior ion rejection rate of the composite membrane, the microscopic behavior of ions was studied. Fig. S5a shows the density profiles of ions along the Z-axis of the simulation system when an external pressure of 50 MPa is applied. The ions were trapped and remained in the feed chamber, and ions could not pass through the membrane region. Because the distribution of ions was affected by both ion and pore sizes, the ion–water radial distribution function (RDF) was subsequently studied to obtain the hydration radius of Na^+ and Cl^-. As shown in Fig. S6, the X-axis value corresponding to the first groove of the cross section of the ion–water RDF was the hydration radius of the ion. The hydration radii of Na^+ and Cl^- were 0.32 and 0.395 nm, respectively, and their hydration diameters were 0.64 and 0.79 nm, respectively. However, the TpPa-1/HPB-COF equivalent pore diameter was 0.525 nm. As shown in Fig. 5, hydration shells surrounding the ions, rendered the ions too large, thus preventing them from passing small cavities as in "petal" nanopores of TpPa-1/HPB-COF composite membrane freely. When the ions were subjected to external pressure, more ions gathered close to the membrane, and only a few ions could pass through the TpPa-1 membrane and enter the composite membrane area. However, the ions could not enter the pure water side, which was consistent with the observation that only a few ions were in the membrane region.

This "petal" pore was attributed to the significant difference between AB-stacked TpPa-1 and TpPa-1/HPB-COF membrane ion retention rate. The effective pore size of the AB-stacked TpPa-1 membrane was smaller than the hydration diameter of the membrane, while its ion rejection rate was only 39.42%. In the model diagram of AB-stacked TpPa-1 in Fig. 3c, the hole of TpPa-1 was divided into three large "diamond" pores. The "petal" pore was more irregular than the "diamond" pore, thus allowing only water molecules to pass through. Hence, the ion rejection rate of TpPa-1/HPB-COF was 100%, which was consistent with the study of Amir et al., which found that nanopores with irregular elongated geometries exhibited a superior ion rejection rate [36]. In addition, the number of water molecules in the solvation shell of Cl^- and Na^+ ions in different membranes demonstrates the difference between AB-stacked TpPa-1 and TpPa-1/HPB-COF membranes. As shown in Figure S7, the coordinate number of ions close to the membrane was smaller than the value in the bulk solution, indicating that dehydration of the first hydration layer for the ions occurred when ions were pressured through the membrane, and the degree of dehydration for ions in TpPa-1/HPB-COF membrane simulation system was larger than that of AB-stacked TpPa-1 membrane. From the perspective of ionic hydration structure change, more energy loss for ions to pass through the TpPa-1/HPB-COF membrane, indicating the ions was more difficult to pass through TpPa-1/HPB-COF.

To verify the superior ion rejection rate of TpPa-1/HPB-COF, one random Na^+ and Cl^- was chosen to display tracking paths during the MD simulation. As shown in Fig. S8, the Na^+ and Cl^-, which cannot completely pass through the composite membrane, moved closer to the middle region of the TpPa-1/HPB-COF along the Z-axis. As shown in

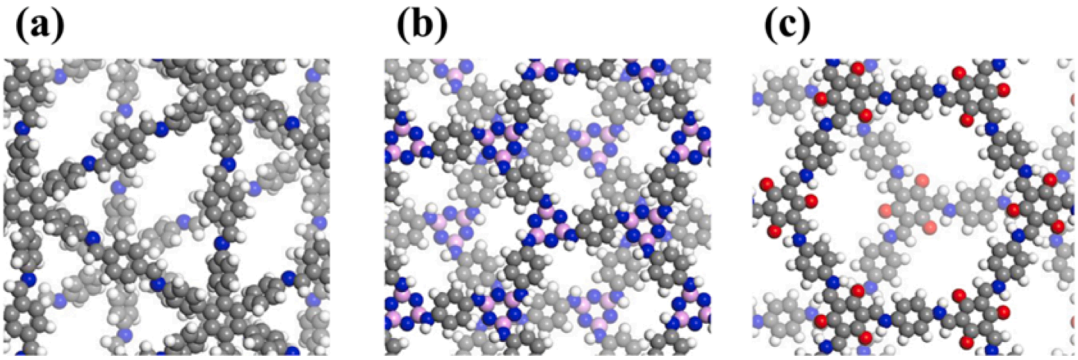

Fig. 3. Illustration of AB-stacking mode of (a) HPB-COF, (b)MPCOF, (c)TpPa-1 multilayers.

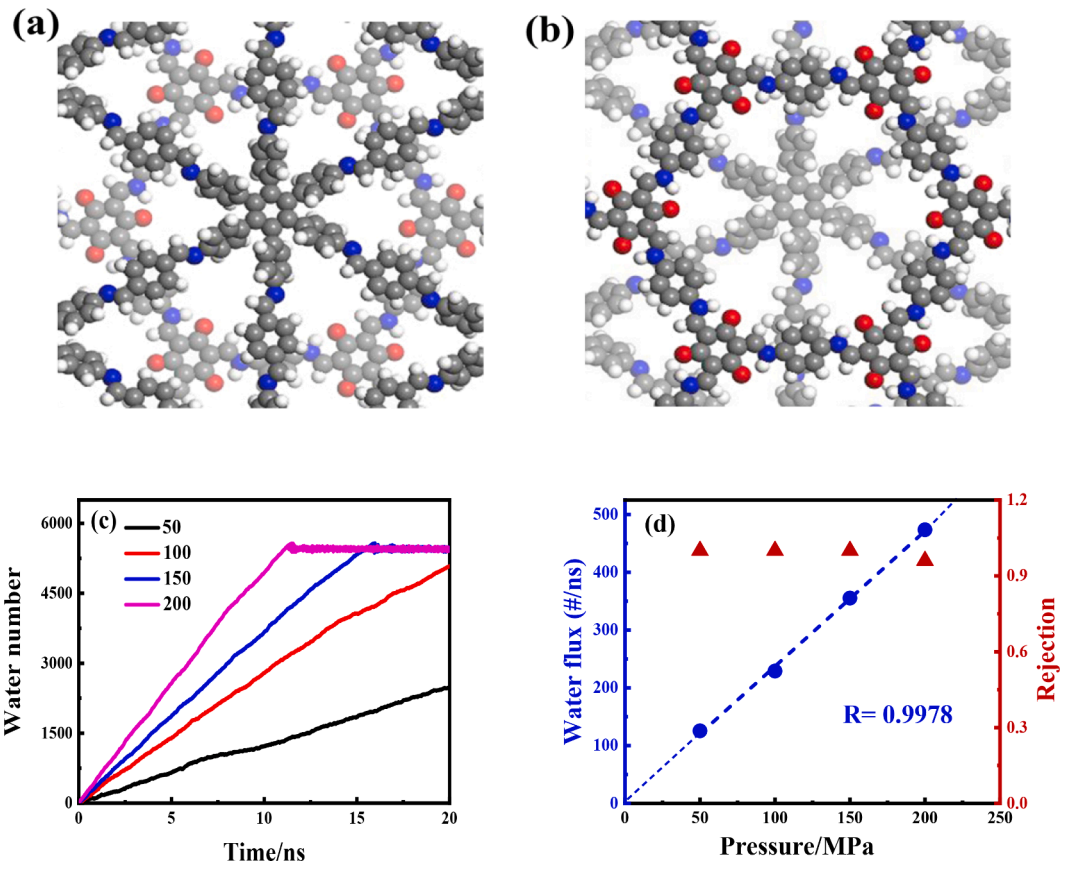

Fig. 4. Illustration of the (a) TpPa-1/HPB-COF, (b) HPB-COF/TpPa-1 composite membrane (c) The number of water molecules filtered through the TpPa-1/HPB-COF membranes and (d) Water flux and salt rejection rate of TpPa-1/HPB-COF with different pressure.

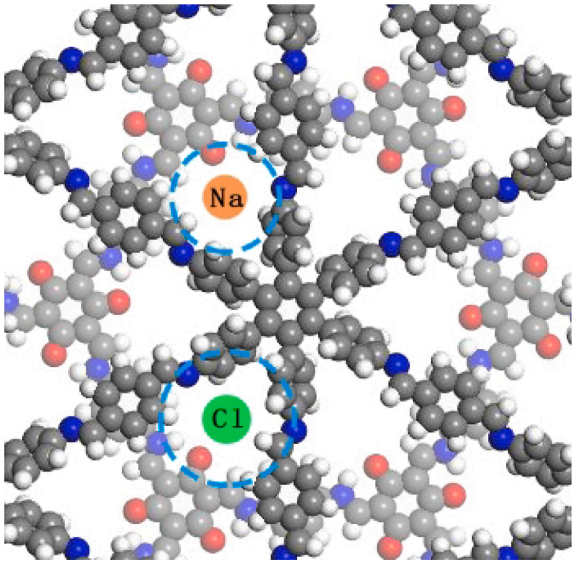

Fig. 5. Scheme of ions with hydration shells being blocked by small cavities in the "petal" pore of TpPa-1/HPB-COF. The blue dashed line represents the extent of the ionic hydration layer. (For interpretation of the references to color in this figure legend, the reader is referred to the web version of this article.)

Fig. 6a, the potential of mean force (PMF) of Na^+ and Cl^- was determined using the Adaptive Biasing Forces (ABF) method [53]. The result showed that the PMF of ions along the Z axis had a high peak in the middle of the membrane, indicating that a high energy barrier prevents the ion from passing through this region.

3.3.2. *Water permeance*

To better present the superior desalination performance of the TpPa-1/HPB-COF composite membrane, we further compared the water permeation rates of AB-stacked HPB-COF, TpPa-1/HPB-COF and AB-stacked TpPa-1. As shown in Fig. 7(a), although the AB-stacked TpPa-1 exhibited the highest water permeation rate, the ion rejection rate was only 39.42%. The number of coordinates for ions in different membranes was calculated to know the reason for the poor ion rejection rate of the AB-stacked TpPa-1 membrane. As shown in Fig. S16, the coordinate number of ions close to the membrane was less than the value in the bulk solution, indicating that dehydration of the first hydration layer for the ions occurred when ions were pressured through the membrane. Compared with the AB-stacked TpPa-1 membrane, the ions required more energy to dehydrate when they passed through the TpPa-1/HPB-COF membrane. The TpPa-1/HPB-COF exhibited a higher water permeation rate while maintaining a 100% ion rejection rate, which is about 1.85 times that of AB-stacked HPB-COF. However, little difference was observed between AB-stacked HPB-COF and TpPa-1/HPB-COF in the effective pore size. In addition, a significant difference was observed in the water permeance, indicating that other factors different from effective pore size affect water permeance.

To better investigate the reasons for the difference between AB-stacked HPB-COF and TpPa-1/HPB-COF in water permeance, the number of water molecules along the Z-axis is plotted in Fig. 7(b). The density of water molecules density in the pores of the TpPa-1/HPB-COF was relatively high, especially in the TpPa-1 part toward the brine side. The high density of water might be attributed to the larger pore size of TpPa-1/HPB-COF. The pore size of TpPa-1/HPB-COF was larger than that of the AB-stacked HPB-COF, and TpPa-1 with a large pore size was located in the first layer with a larger accessible surface area, facilitating the movement of more water molecules to the membrane area at the

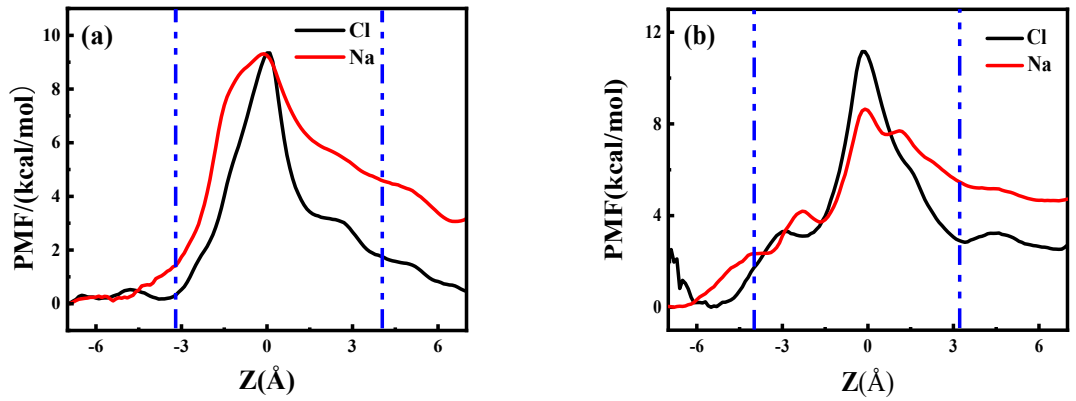

Fig. 6. Potential of mean force for ions in (a) TpPa-1/HPB-COF and (b) HPB-COF/TpPa-1 composite membrane.

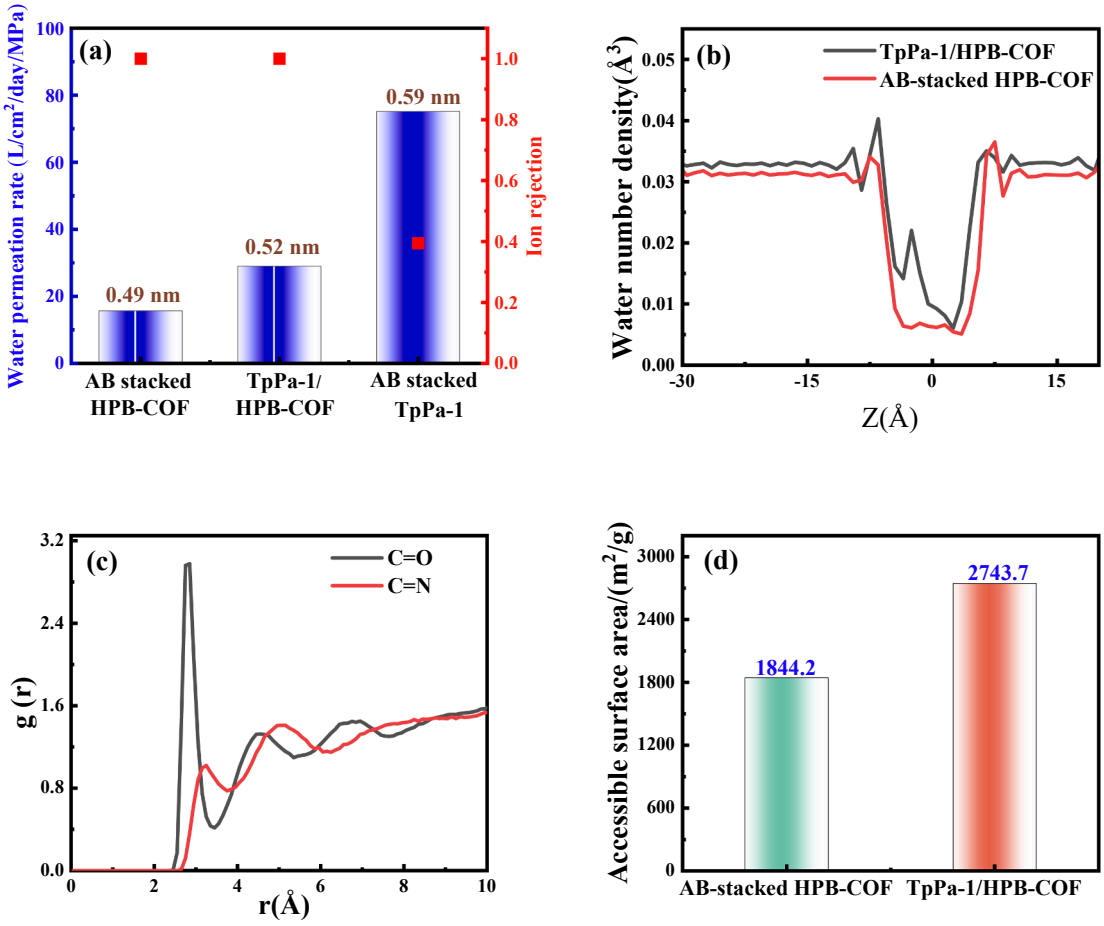

Fig. 7. Desalination performance of (a) AB-stacked HPB-COF, TpPa-1/ HPB-COF and TpPa-1 membranes (b) Number density profile of water molecules along the Z-axis, (c) RDF between functional group (C═O: O and C═N: N) and oxygen atoms from water molecules and (d) The accessible surface area of AB-stacked HPB-COF and TpPa-1/ HPB-COF.

same time. Except for the large pore size, according to the characterization of TpPa-1 structure by Thomas et al., the existence of hydrophilic group C═O in TpPa-1 was verified [42]. The hydrophilic group C═O in the TpPa-1 membrane is attributed to the presence of higher peaks, and its hydrophilic characteristics attract more water molecules to gather close to the membrane, which is beneficial to improve the water flux. Further evidence for the hydrophilicity of C═O was obtained by plotting the RDF between the groups and the water molecules (Fig. 7c). The C═N on HPB-COF was compared with the C═O, and the peak of the C═O was higher than that of C═N. The higher peak indicates that the interaction between the C═O and water molecules is stronger than C═N and attracts more water molecules into the membrane region.

The distribution density of water molecules inside the composite membrane was further analyzed using Multiwfn [54], (Fig. 8). The analysis revealed that the density distribution of water molecules in the TpPa-1/HPB-COF composite membrane was higher than that of the AB-stacked HPB-COF. Compared with the density map of the TpPa-1 and HPB-COF monolayers (Fig. 8a–b), the density map of the TpPa-1/HPB-COF showed that the “hexagonal star” of TpPa-1 was divided into a “round stamen” and six “small petals”. The path of water molecules

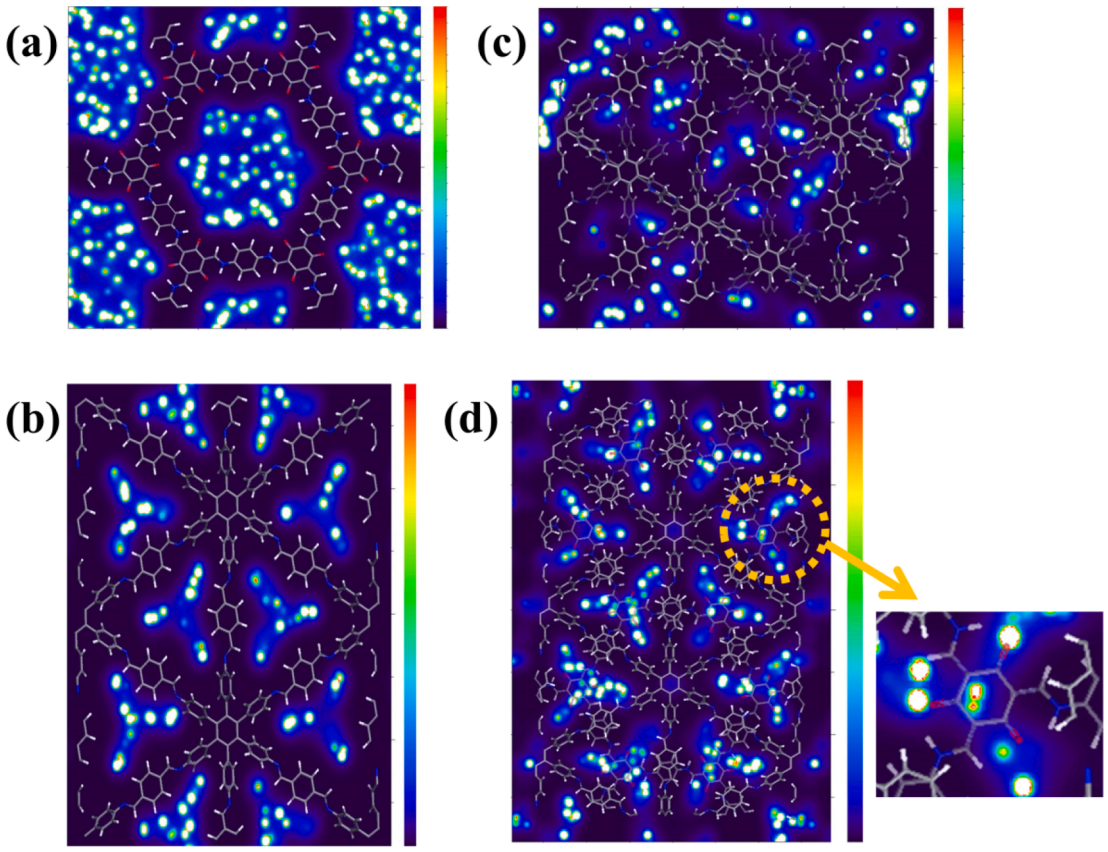

Fig. 8. The *x-y* plane average density distribution of water molecules inside the (a) TpPa-1, (b) HPB-COF, (c) AB-stacked HPB-COF, and (d) TpPa-1/HPB-COF.

through the composite membrane can be determined by comparing the density distribution. In particular, a high-density region was observed around each C═O, indicating that more water molecules were gathered nearby, further confirming that C═O was more hydrophilic and could attract water molecules into the membrane area.

In addition to the contributions of hydrophilic C═O and the pore size of TpPa-1, the other characteristics contributing to the superior water permeance of TpPa-1/HPB-COF were deeply explored. The available surface area of the TpPa-1/HPB-COF was larger than that of the AB-stacked HPB-COF. As shown in Fig. 7(d), the available surface area of the TpPa-1/HPB-COF was up to 2743.70 m^2/g, while that of the AB-stacked HPB-COF was 1844.18 m^2/g, which is about 1.49 times larger discrepancy. The larger available surface area provides a bigger platform allowing the water molecules to enter the pure water sides, thus improving the water permeation rate.

The interaction between the pore wall and water molecules is a major factor in the dynamic random motion of water molecules. The dynamics of in-pore water molecules can be characterized using the self-diffusion coefficient along the z-direction (Dz). The mean-squared displacements of all in-pore water molecules in the z-direction (MSDz) should be first measured to calculate Dz. Dz can be calculated using Equation (4):

$$Dz = \frac{lim MSDz(t)}{2t} \quad (4)$$

The alteration of MSDz with time in the AB-stacked HPB-COF and TpPa-1/HPB-COF composite membrane is shown in Fig. 9a. The Dz value of the TpPa-1/HPB-COF composite membrane was $0.124 \cdot 10^{-9}$

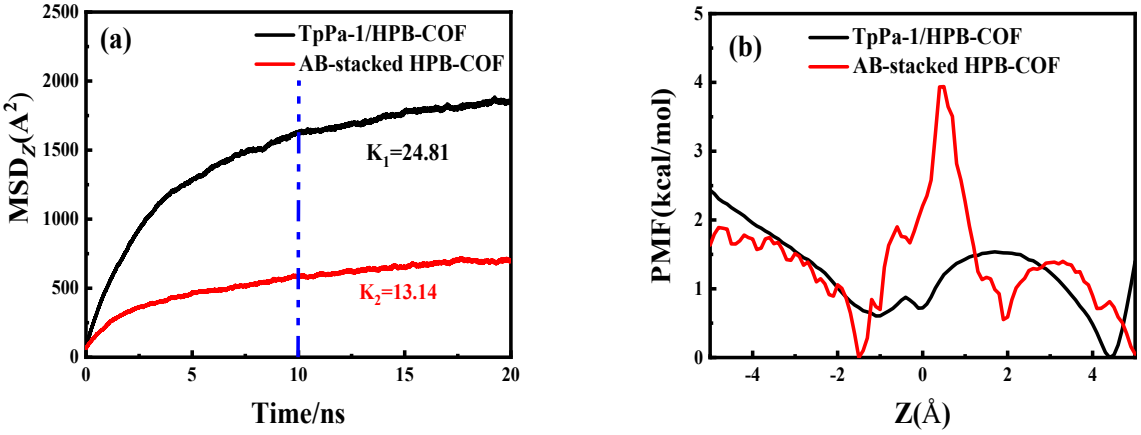

Fig. 9. (a) Mean-square displacements along the z direction of water molecules and (b) PMF for water molecules of AB-stacked HPB-COF and TpPa-1/ HPB-COF.

$m^2 \cdot s^{-1}$, while the Dz value of AB-stacked HPB-COF was $0.066 \cdot 10^{-9}$ $m^2 \cdot s^{-1}$, which is about 1.88 times higher than that of AB-stacked HPB-COF.

The PMF of the water molecules along the Z-axis was calculated to describe the free energy profile of water molecules transported through the TpPa-1/HPB-COF, as shown in (Fig. 9b), and the peak of PMF curves spanning the AB-stacked HPB-COF was higher than that of the TpPa-1/HPB-COF, indicating that AB-stacked HPB-COF had a stronger energy barrier when water molecules passed through the membrane, resulting in poor water permeation.

3.3.3. Comparison between HPB-COF/TpPa-1 and TpPa-1/HPB-COF membrane

The model with the HPB-COF of the composite membrane placed toward the feed side (referred to as HPB-COF/TpPa-1), shown in Fig. 4b, was also established to explore whether the position of the membrane with different pore sizes would affect desalination performance. The water permeance and ion rejection rate are calculated from the data after 10 ns, indicating that the desalination performance is not affected by the position of the membrane with different pore sizes (Fig. S11). Almost all ions remained in the feed chamber, and few ions were observed in the membrane zone (Fig. S5b). As shown in Fig. 6b, the PMF of ions along the Z-axis also had a high peak in the middle of the HPB-COF/TpPa-1, reflecting the excellent ion rejection of HPB-COF/TpPa-1. Ben et al. reported that the free energy barriers could be attributed to the energy needed to (partially) dehydrate the ions [55]. By comparing the calculated coordination number of water molecules of ions in bulk solution and ions close to the HPB-COF/TpPa-1 membrane, the number of coordinates for ions close to HPB-COF/TpPa-1 membrane was less than that of the bulk solution, indicating the dehydration occurred when the ions accessed the membrane (Fig. S10). The existence of high energy barrier in the middle of HPB-COF/TpPa-1 indicated that more energy loss for ions to pass through the composite membrane. Hence, ions could not pass through the membrane region. In addition, the variation in MSDz of the HPB-COF/TpPa-1 is similar to that of the TpPa-1/HPB-COF composite membrane (Fig. S14). The similarity in MSDz variation confirms that the performance of HPB-COF/TpPa-1 is not affected when the position of the membrane with different pore sizes changes. As shown in Fig. S9, the water flux of HPB-COF/TpPa-1 is low before 10 ns, and the performance tends to be stable after 10 ns. The early performance of membrane HPB-COF/TpPa-1 is not stable, which may be attributed to the small HPB-COF pore and the lack of hydrophilic C═O, resulting in insufficient water molecules entering the membrane region. When TpPa-1 is located on the brine side (Fig. S12), its density is significantly higher than that of HPB-COF, which allows more water molecules to enter the membrane area in the same amount of time to quickly reach a steady state. Apart from this, a similar finding is also displayed in Fig. S13. From the density distribution of water molecules along the Y axis, we can obtain the location of the interlayer pathways of water molecules. A higher density region was observed close to the TpPa-1 of TpPa-1/HPB-COF, which was consistent with the above observations.

3.4. Effect of layer spacing on performance

The interlayer spacing of the TpPa-1/HPB-COF membrane was adjusted to determine the optimal separation size for desalination performance. Fig. 10a shows the time evolution of the number of water molecules passing through the TpPa-1/HPB-COF membrane with different interlayer spacing under a pressure of 50 MPa. The slope increased as the layer spacing increased. Fig. 10b shows the excellent desalination performance of the TpPa-1/HPB-COF membrane when the layer spacing is adjusted at 0.44 nm.

To better understand the effect of layer spacing on desalination performance, the number density of water molecules is plotted in Fig. S15. The density in the composite membrane region increased as the layer spacing increased, particularly at 0.54 nm. A higher peak was observed in the membrane region, indicating more water molecules entered the membrane region simultaneously and also indicated that the water permeability of the membrane region improved. As shown in Fig. S16, the density distribution widened with the increasing layer spacing, which is consistent with the above results.

The number density of ions along the Z-axis was also plotted to provide more detailed information about the effect of the layer spacing on ion rejection rate. As shown in Fig. S17, no ion was observed on permeation sides when the layer spacing was 0.34 and 0.44 nm. When the layer spacing increased to 0.54 nm, a few ions completely passed through the composite membrane to the permeation side. As shown in Fig. S17d, as the layer spacing increased, the degree of ion dehydration in the membrane decreased. This phenomenon is because the increase in the distance between two layers of the film reduces the influence on ions.

To comprehensively show the significant potential of the TpPa-1/HPB-COF composite membrane used as an RO membrane, we further compared the desalination performance of the composite membrane with that of commercial membranes (MFI-type zeolite [56], and commercial RO [24]) and other nanomaterials (MoS_2 [57], $MoSe_2$[24], Asn func. SWCNTs [58], AlSiNT [59], and Graphene [57]). TpPa-1/HPB-COF composite membrane with a layer spacing of 0.44 nm exhibited superior salt rejection rate and water permeation rate (Fig. 11), with water permeation rate is increased at 40.04 $L/cm^2/day/MPa$.

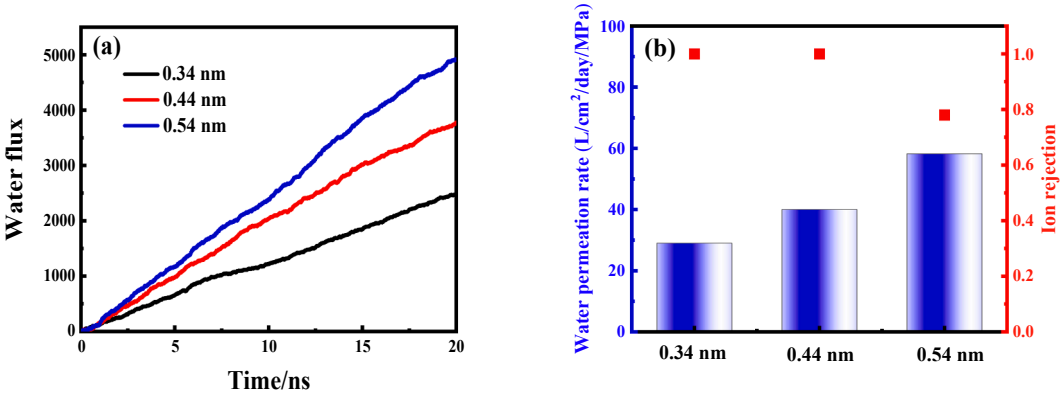

Fig. 10. (a) The number of water molecules filtered through the TpPa-1/HPB-COF membrane. (b) Desalination performance of TpP-1/HPB-COF membrane with different layer spacing.

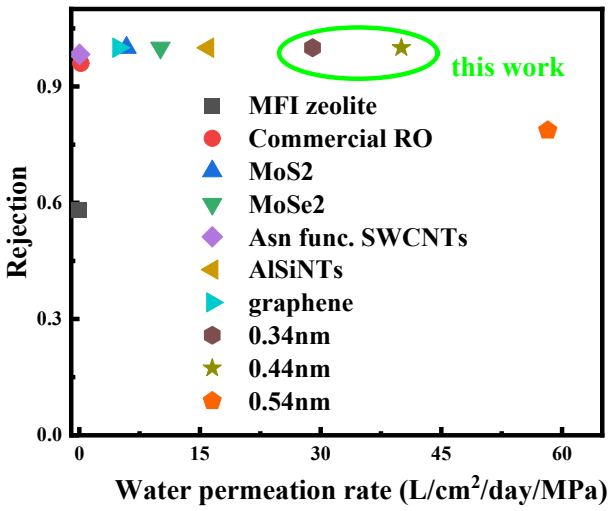

Fig. 11. The comparison in desalination performance of TpPa-1/HPB-COF with various membranes.

4. Conclusion

In this study, we investigated the properties of the petal-shaped composite membrane formed by superimposing COF with a large aperture difference from a microscopic perspective. Through NEMD simulations, the desalination performance of COF multilayer membranes with different pore sizes was investigated. HPB-COF, MPCOF and TpPa-1 with intrinsic pores of 0.577, 0.978 and 1.582 nm, respectively, were chosen to represent COFs with different pore sizes for desalination. However, the ion rejection rate of monolayer COF as an RO membrane was poor. The AB-stacked mode reduced the effective pore size and increased the ion retention rate, thereby reducing water permeability. The TpPa-1/HPB-COF membrane exhibited a salt rejection rate of 100% and water permeance of 29.00 L/cm^2/day/MPa, which is about 1.85 times that of the AB-stacked HPB-COF. Through simulation analysis, we found that stacking COF materials with different pore sizes and types to form composite membranes could simultaneously achieve high water permeance and salt rejection rate. The separation performance of the composite was affected by the available surface area, pore size, and functional group nature of the COF membrane. The optimal interlayer spacing of the TpPa-1/HPB-COF composite was 0.44 nm for seawater desalination. Hence, this study may help researchers to understand the effect of material designs on desalination performance at different operating conditions and from molecular perspectives.

CRediT authorship contribution statement

Mengjiao Guan: Writing – original draft, Methodology. **Dengfeng Yang:** Writing – review & editing, Methodology. **Qing Li:** Formal analysis. **Huiting Zhang:** Visualization. **Jianan Xu:** Visualization. **Mengmeng Cai:** Validation. **Weike Lin:** Validation. **Shengqian Ma:** Writing – review & editing. **Qingzhi Liu:** Supervision, Resources.

Declaration of Competing Interest

The authors declare that they have no known competing financial interests or personal relationships that could have appeared to influence the work reported in this paper.

Data availability

Data will be made available on request.

Acknowledgement

This research was funded by the National Natural Science Foundation of Shandong Province (No.ZR2019MB020 and ZR2020MB119), Applied Research Project of Qingdao Postdoctoral (01020240119), and China Postdoctoral Science Foundation (2022M720083).

Appendix. Supplementary material A

Supplementary data to this article can be found online at https://doi.org/10.1016/j.apsusc.2023.156441.

References

[1] K. Zhang, Z. He, K.M. Gupta, et al., Computational design of 2D functional covalent–organic framework membranes for water desalination[J], Environ. Sci. Water Res. Technol. 3 (4) (2017) 735–743, https://doi.org/10.1039/C7EW00074J.
[2] A.E. Ercin, A.Y. Hoekstra, Water footprint scenarios for 2050: A global analysis[J], Environ. Int. 64 (2014) 71–82, https://doi.org/10.1016/j.envint.2013.11.019.
[3] M.M. Mekonnen, A.Y. Hoekstra, Four billion people facing severe water scarcity [J], Sci. Adv. 2 (2) (2016) e1500323.
[4] M. Laqbaqbi, J.A. Sanmartino, M. Khayet, et al., Fouling in membrane distillation, osmotic distillation and osmotic membrane distillation[J], Appl. Sci. 7 (4) (2017) 334, https://doi.org/10.3390/app7040334.
[5] L.F. Dumée, H. Alglave, T. Chaffraix, et al., Morphology-properties relationship of gas plasma treated hydrophobic meso-porous membranes and their improved performance for desalination by membrane distillation[J], Appl. Surf. Sci. 363 (2016) 273–285, https://doi.org/10.1016/j.apsusc.2015.12.034.
[6] L. García-Fernández, C. García-Payo, M. Khayet, Hollow fiber membranes with different external corrugated surfaces for desalination by membrane distillation[J], Appl. Surf. Sci. 416 (2017) 932–946, https://doi.org/10.1016/j.apsusc.2017.04.232.
[7] B.J. KatoáZ, K.I.K. HashimotoáK, Durability enhancement and degradation of oxygen evolution anodes in seawater electrolysis for hydrogen production[J], Appl. Surf. Sci. 257 (2011) 8230–8236, https://doi.org/10.1016/j.apsusc.2010.12.042.
[8] Y. Xue, J. Zhao, R. Qiu, et al., In situ glass antifouling using Pt nanoparticle coating for periodic electrolysis of seawater[J], Appl. Surf. Sci. 357 (2015) 60–68, https://doi.org/10.1016/j.apsusc.2015.08.232.
[9] M. Tsai, L. Chung, G. Lin, et al., Layered carbon nanotube/polyacrylonitrile thin-film composite membrane for forward osmosis application[J], Sep. Purif. Technol. 241 (2020), 116683, https://doi.org/10.1016/j.seppur.2020.116683.
[10] J. Shi, H. Kang, N. Li, et al., Chitosan sub-layer binding and bridging for nanofiber-based composite forward osmosis membrane[J], Appl. Surf. Sci. 478 (2019) 38–48, https://doi.org/10.1016/j.apsusc.2019.01.148.
[11] H. Yang, Z. Zhang, Y. Wang, Cavitating substrates to boost water permeance of reverse osmosis membranes[J], Sep. Purif. Technol. 299 (2022), 121810, https://doi.org/10.1016/j.seppur.2022.121810.
[12] K. Matshetshe, K. Sikhwivhilu, G. Ndlovu, et al., Antifouling and antibacterial β-cyclodextrin decorated graphene oxide/polyamide thin-film nanocomposite reverse osmosis membranes for desalination applications[J], Sep. Purif. Technol. 278 (2021), 119594, https://doi.org/10.1016/j.seppur.2021.119594.
[13] J. Benecke, J. Rozova, M. Ernst, Anti-scale effects of select organic macromolecules on gypsum bulk and surface crystallization during reverse osmosis desalination[J], Sep. Purif. Technol. 198 (2018) 68–78, https://doi.org/10.1016/j.seppur.2016.11.068.
[14] A.W. Mohammad, Y.H. Teow, W.L. Ang, et al., Nanofiltration membranes review: Recent advances and future prospects[J], Desalination 356 (2015) 226–254, https://doi.org/10.1016/j.desal.2014.10.043.
[15] L. Wang, M.S.H. Boutilier, P.R. Kidambi, et al., Fundamental transport mechanisms, fabrication and potential applications of nanoporous atomically thin membranes[J], Nat. Nanotechnol. 12 (6) (2017) 509–522, https://doi.org/10.1038/nnano.2017.72.
[16] D. Li, Y. Yan, H. Wang, Recent advances in polymer and polymer composite membranes for reverse and forward osmosis processes[J], Prog. Polym. Sci. 61 (2016) 104–155, https://doi.org/10.1016/j.progpolymsci.2016.03.003.
[17] J.R. Werber, C.O. Osuji, M. Elimelech, Materials for next-generation desalination and water purification membranes[J], Nat. Rev. Mater. 1 (5) (2016) 1–15, https://doi.org/10.1038/natrevmats.2016.18.
[18] Z. Zhao, J. Jiang, POC/PIM-1 mixed-matrix membranes for water desalination: A molecular simulation study[J], J. Membr. Sci. 608 (2020), 118173, https://doi.org/10.1016/j.memsci.2020.118173.
[19] S.C. O'Hern, M.S.H. Boutilier, J.C. Idrobo, et al., Selective ionic transport through tunable subnanometer pores in single-layer graphene membranes[J], Nano Lett. 14 (3) (2014) 1234–1241, https://doi.org/10.1021/nl404118f.
[20] Y. Zhang, T. Fang, Q. Hou, et al., Water desalination of a new three-dimensional covalent organic framework: a molecular dynamics simulation study[J], PCCP 22 (29) (2020) 16978–16984, https://doi.org/10.1039/D0CP01792B.
[21] P.J.J. Alvarez, C.K. Chan, M. Elimelech, et al., Emerging opportunities for nanotechnology to enhance water security[J], Nat. Nanotechnol. 13 (8) (2018) 634–641, https://doi.org/10.1038/s41565-018-0203-2.

[22] D. Yang, Q. Li, J. Shi, et al., Inner surface modification of 1.76 nm diameter (13, 13) carbon nanotubes and the desalination behavior of its reverse osmosis membrane[J], New J. Chem. 41 (23) (2017) 14325–14333, https://doi.org/10.1039/C7NJ02466E.
[23] Q. Li, Q. Liu, M. Guan, et al., Molecular simulation of modified large interstice outer wall carbon nanotube membrane and its desalination behavior[J], Appl. Surf. Sci. (2022:), 153812, https://doi.org/10.1016/j.apsusc.2022.153812.
[24] J.W. Shen, J. Li, F. Liu, et al., A molecular dynamics study on water desalination using single-layer MoSe2 nanopore[J], J. Membr. Sci. 595 (2020), 117611, https://doi.org/10.1016/j.memsci.2019.117611.
[25] X. Ma, X. Zhu, C. Huang, et al., Revealing the effects of terminal groups of MXene on the water desalination performance[J], J. Membr. Sci. 647 (2022), 120334, https://doi.org/10.1016/j.memsci.2022.120334.
[26] X.L. Cao, J.L. Guo, J. Cai, et al., The encouraging improvement of polyamide nanofiltration membrane by cucurbituril-based host–guest chemistry[J], AIChE J 66 (4) (2020), e16879, https://doi.org/10.1002/aic.16879.
[27] N.A. Khan, H. Wu, Y. Jinqiu, et al., Incorporating covalent organic framework nanosheets into polyamide membranes for efficient desalination[J], Sep. Purif. Technol. 274 (2021), 119046, https://doi.org/10.1016/j.seppur.2021.119046.
[28] Z. Zhang, C. Yin, X. Shi, et al., Masking covalent organic frameworks (COFs) with loose polyamide networks for precise nanofiltration[J], Sep. Purif. Technol. 283 (2022), 120233, https://doi.org/10.1016/j.seppur.2021.120233.
[29] L. Ni, K. Chen, J. Xie, et al., Synchronizing formation of polyamide with covalent organic frameworks towards thin film nanocomposite membrane with enhanced nanofiltration performance[J], J. Membr. Sci. 646 (2022), 120253, https://doi.org/10.1016/j.memsci.2022.120253.
[30] J. Shen, J. Yuan, B. Shi, et al., Homointerface covalent organic framework membranes for efficient desalination[J], J. Mater. Chem. A 9 (40) (2021) 23178–23187, https://doi.org/10.1039/D1TA06439H.
[31] Z. Qu, C. Lai, G. Zhao, et al., Pore engineering in covalent organic framework membrane for gas separation[J], Advanced Membranes 2 (2022), 100037, https://doi.org/10.1016/j.advmem.2022.100037.
[32] C. Liu, Y. Jiang, A. Nalaparaju, et al., Post-synthesis of a covalent organic framework nanofiltration membrane for highly efficient water treatment[J], J. Mater. Chem. A 7 (42) (2019) 24205–24210, https://doi.org/10.1039/C9TA06325K.
[33] A. Xiao, X. Shi, Z. Zhang, et al., Secondary growth of bi-layered covalent organic framework nanofilms with offset channels for desalination[J], J. Membr. Sci. 624 (2021), 119122, https://doi.org/10.1016/j.memsci.2021.119122.
[34] W. Zhou, M. Wei, X. Zhang, et al., Fast desalination by multilayered covalent organic framework (COF) nanosheets[J], ACS Appl. Mater. Interfaces 11 (18) (2019) 16847–16854, https://doi.org/10.1021/acsami.9b01883.
[35] M. Wei, W. Zhou, F. Xu, et al., Nanofluidic behaviors of water and ions in covalent triazine framework (CTF) multilayers[J], Small 16 (9) (2020) 1903879, https://doi.org/10.1002/smll.201903879.
[36] Z. Cao, G. Markey, F.A. Barati, Ozark graphene nanopore for efficient water desalination[J], J. Phys. Chem. B 125 (40) (2021) 11256–11263, https://doi.org/10.1021/acs.jpcb.1c06327.
[37] K. Dey, M. Pal, K.C. Rout, et al., Selective molecular separation by interfacially crystallized covalent organic framework thin films[J], J. Am. Chem. Soc. 139 (37) (2017) 13083–13091, https://doi.org/10.1021/jacs.7b06640.
[38] J. Yang, B. Tu, G. Zhang, et al., Advancing osmotic power generation by covalent organic framework monolayer, Nat. Nanotechnol. 17 (2022) 622–628, https://doi.org/10.1038/s41565-022-01110-7.
[39] F. Pan, W. Guo, Y. Su, et al., Direct growth of covalent organic framework nanofiltration membranes on modified porous substrates for dyes separation[J], Sep. Purif. Technol. 215 (2019) 582–589, https://doi.org/10.1016/j.seppur.2019.01.064.
[40] S. Dalapati, M. Addicoat, S. Jin, et al., Rational design of crystalline supermicroporous covalent organic frameworks with triangular topologies[J], Nat. Commun. 6 (1) (2015) 1–8, https://doi.org/10.1038/ncomms8786.
[41] S. Zhang, X. Zhao, B. Li, et al., “Stereoscopic” 2D super-microporous phosphazene-based covalent organic framework: design, synthesis and selective sorption towards uranium at high acidic condition[J], J. Hazard. Mater. 314 (2016) 95–104, https://doi.org/10.1016/j.jhazmat.2016.04.031.
[42] S. Kandambeth, A. Mallick, B. Lukose, et al., Construction of crystalline 2D covalent organic frameworks with remarkable chemical (acid/base) stability via a combined reversible and irreversible route[J], J. Am. Chem. Soc. 134 (48) (2012) 19524–19527, https://doi.org/10.1021/ja308278w.
[43] Y. Lan, M. Tong, Q. Yang, et al., Computational screening of covalent organic frameworks for the capture of radioactive iodine and methyl iodide[J], CrstEngComm 19 (33) (2017) 4920–4926, https://doi.org/10.1039/C7CE00118E.
[44] L.C. Lin, J.C. Grossman, Atomistic understandings of reduced graphene oxide as an ultrathin-film nanoporous membrane for separations[J], Nat. Commun. 6 (1) (2015) 1–7, https://doi.org/10.1038/ncomms9335.
[45] Z. Cao, V. Liu, F.A. Barati, Water desalination with two-dimensional metal–organic framework membranes[J], Nano Lett. 19 (12) (2019) 8638–8643, https://doi.org/10.1021/acs.nanolett.9b03225.
[46] X. Zhang, M. Wei, F. Xu, et al., Pressure-Dependent Ion Rejection in Nanopores[J], J. Phys. Chem. C 124 (37) (2020) 20498–20505, https://doi.org/10.1021/acs.jpcc.0c03641.
[47] S. Plimpton, Fast parallel algorithms for short-range molecular dynamics[J], J. Comput. Phys. 117 (1) (1995) 1–19, https://doi.org/10.1006/jcph.1995.1039.
[48] M. Kargar, A. Lohrasebi, Deformation of water nano-droplets on graphene under the influence of constant and alternative electric fields[J], PCCP 19 (39) (2017) 26833–26838, https://doi.org/10.1039/C7CP04433J.
[49] M. Tong, Q. Yang, Y. Xiao, et al., Revealing the structure–property relationship of covalent organic frameworks for CO_2 capture from postcombustion gas: a multi-scale computational study[J], PCCP 16 (29) (2014) 15189–15198, https://doi.org/10.1039/C4CP02047B.
[50] M. Tong, Q. Yang, Q. Ma, et al., Few-layered ultrathin covalent organic framework membranes for gas separation: a computational study[J], J. Mater. Chem. A 4 (1) (2016) 124–131, https://doi.org/10.1039/C5TA06707C.
[51] I.S. Joung, T.E. Cheatham III, Determination of alkali and halide monovalent ion parameters for use in explicitly solvated biomolecular simulations[J], J. Phys. Chem. B 112 (30) (2008) 9020–9041, https://doi.org/10.1021/jp8001614.
[52] T.F. Willems, C.H. Rycroft, M. Kazi, et al., Algorithms and tools for high-throughput geometry-based analysis of crystalline porous materials[J], Microporous Mesoporous Mater. 149 (1) (2012) 134–141, https://doi.org/10.1016/j.micromeso.2011.08.020.
[53] D. Yang, Q. Liu, H. Li, et al., Molecular simulation of carbon nanotube membrane for Li^+ and Mg^{2+} separation[J], J. Membr. Sci. 444 (2013) 327–331, https://doi.org/10.1016/j.memsci.2013.05.019.
[54] T. Lu, F. Chen, Multiwfn: a multifunctional wavefunction analyzer[J], J. Comput. Chem. 33 (5) (2012) 580–592, https://doi.org/10.1002/jcc.22885.
[55] C. Song, B. Corry, Intrinsic ion selectivity of narrow hydrophobic pores[J], J. Phys. Chem. B 113 (21) (2009) 7642–7649, https://doi.org/10.1021/jp810102u.
[56] L. Li, J. Dong, T.M. Nenoff, et al., Desalination by reverse osmosis using MFI zeolite membranes[J], J. Membr. Sci. 243 (1–2) (2004) 401–404, https://doi.org/10.1016/j.memsci.2004.06.045.
[57] M. Heiranian, A.B. Farimani, N.R. Aluru, Water desalination with a single-layer MoS2 nanopore[J], Nat. Commun. 6 (1) (2015) 1–6, https://doi.org/10.1038/ncomms9616.
[58] A. Güvensoy-Morkoyun, S. Velioğlu, M.G. Ahunbay, et al., Desalination potential of aquaporin-inspired functionalization of carbon nanotubes: bridging between simulation and experiment[J], ACS Appl. Mater. Interfaces (2022), https://doi.org/10.1021/acsami.2c03700.
[59] K.H. Liou, D.Y. Kang, L.C. Lin, Investigating the potential of single-walled aluminosilicate nanotubes in water desalination[J], ChemPhysChem 18 (2) (2017) 179–183, https://doi.org/10.1002/cphc.201600900.